New Journal of Physics
The open access journal at the forefront of physics

Deutsche Physikalische Gesellschaft DPG IOP Institute of Physics

PAPER • OPEN ACCESS

# Energy absorption and coupling to electrons in the transition from surface- to volume-dominant intense laser–plasma interaction regimes

Recent citations

- Self-Referencing Spectral Interferometric Probing of the Onset Time of Relativistic Transparency in Intense Laser-Foil Interactions
S.D.R. Williamson *et al*

To cite this article: S D R Williamson *et al* 2020 *New J. Phys.* **22** 053044

View the article online for updates and enhancements.

This content was downloaded from IP address 109.175.189.32 on 23/09/2020 at 17:19

New Journal of Physics
The open access journal at the forefront of physics

Deutsche Physikalische Gesellschaft DPG
IOP Institute of Physics

Published in partnership with: Deutsche Physikalische Gesellschaft and the Institute of Physics

OPEN ACCESS

RECEIVED
21 December 2019

REVISED
12 March 2020

ACCEPTED FOR PUBLICATION
6 April 2020

PUBLISHED
27 May 2020

Original content from this work may be used under the terms of the Creative Commons Attribution 4.0 licence.

Any further distribution of this work must maintain attribution to the author(s) and the title of the work, journal citation and DOI.

PAPER

# Energy absorption and coupling to electrons in the transition from surface- to volume-dominant intense laser–plasma interaction regimes

S D R Williamson[1], R J Gray[1], M King[1], R Wilson[1], R J Dance[1], C Armstrong[1,2], D R Rusby[1,2], C Brabetz[3], F Wagner[3], B Zielbauer[3], V Bagnoud[3], D Neely[1,2] and P McKenna[1]

[1] SUPA Department of Physics, University of Strathclyde, Glasgow G4 0NG, United Kingdom
[2] Central Laser Facility, STFC Rutherford Appleton Laboratory, Oxfordshire OX11 0QX, United Kingdom
[3] Plasma Physics Department, GSI Helmholtz Zentrum fuer Schwerionenforschung GmbH, D-64291 Darmstadt, Germany

**E-mail:** paul.mckenna@strath.ac.uk

**Keywords:** intense laser–solid interactions, laser absorption in dense plasma, relativistic self induced transparency

Supplementary material for this article is available online

## Abstract

The coupling of laser energy to electrons is fundamental to almost all topics in intense laser–plasma interactions, including laser-driven particle and radiation generation, relativistic optics, inertial confinement fusion and laboratory astrophysics. We report measurements of total energy absorption in foil targets ranging in thickness from 20 $\mu$m, for which the target remains opaque and surface interactions dominate, to 40 nm, for which expansion enables relativistic-induced transparency and volumetric interactions. We measure a total peak absorption of ~80% at an optimum thickness of ~380 nm. For thinner targets, for which some degree of transparency occurs, although the total absorption decreases, the number of energetic electrons escaping the target increases. 2D particle-in-cell simulations indicate that this results from direct laser acceleration of electrons as the intense laser pulse propagates within the target volume. The results point to a trade-off between total energy coupling to electrons and efficient acceleration to higher energies.

## 1. Introduction

Energy absorption and coupling to electrons in dense targets irradiated by high intensity laser pulses is fundamentally important to the development of ultra-bright sources of high energy ions [1, 2], neutrons [3, 4], positrons [5, 6] and photons [7], to advanced schemes for inertial confinement fusion [8], and in the generation of transient states of warm dense matter [9, 10]. The efficiency with which laser energy is coupled to electrons within the plasma is a crucial aspect in optimising the properties of the particles and radiation generated. The electrons accelerated by the laser directly produce photons and positrons, and their displacement establishes the strong electrostatic fields responsible for ion acceleration. The case of laser energy absorption and coupling to electrons in ultrathin foil targets is particularly interesting. Such targets have been shown to result in ion acceleration to high energies [11–13], with beam properties affected by the transmission of laser light [14, 15] and the formation of electron jets (or filaments) [13, 16–18].

Ping *et al* [19] reports the first direct measurements of laser energy absorption in relativistically intense laser–solid interactions. The targets were Al foils with thickness in the range 1.5–100 $\mu$m and the intensity of the 150 fs-duration laser pulses was varied in the range $10^{17}$ to $10^{20}$ Wcm$^{-2}$. The results show an enhanced absorption at the highest intensities, reaching 60% for near-normal incidence and 80%–90% for

© 2020 The Author(s). Published by IOP Publishing Ltd on behalf of the Institute of Physics and Deutsche Physikalische Gesellschaft

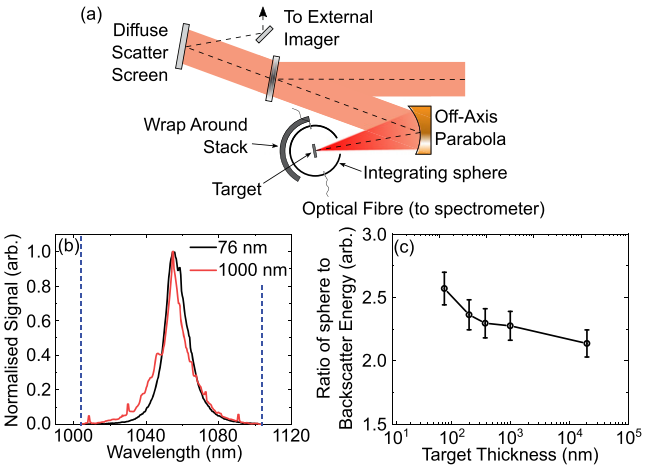


**Figure 1.** (a) Schematic of the experiment arrangement used to determine the degree of laser energy absorbed via measurement of the unabsorbed light fraction. The beam path to the focus at the target surface is shown, along with the integrating sphere and diffuse scatter screen diagnostics used to measure the reflected laser light. The electrons accelerated from the target are characterised using a 'wrap-around' stack of Image Plate. (b) Spectrum of the light diffusely scattered by the target and collected by the integrating sphere, for two example target thicknesses. The spectral region bounded by the dashed lines is used in the integration (±50 nm with respect to the laser central wavelength). (c) Ratio of the energy measured in the integrating sphere to the backscattered energy as function of target thickness.

45° incidence. Gray *et al* [20] reports on total energy absorption measurements for Al foils with thickness in the range 6–20 $\mu$m, for a similar intensity range, but for longer laser pulse duration (∼700 fs) to explore the role of the recirculation of electrons within the foil on absorption [21]. In both of these studies, the targets remain opaque to the laser light, resulting in reflection and energy coupling to electrons via processes such as resonance absorption and $\mathbf{J} \times \mathbf{B}$ heating [22], primarily in the region of the critical density surface. At this surface, the plasma frequency, $\omega_{pe} = (\sqrt{n_e e^2/\gamma_e \epsilon_0 m_e}$, where $-e$, $n_e$, $m_e$ and $\gamma_e$ are the electron charge, density, rest mass and Lorentz factor, respectively, and $\epsilon_0$ is the vacuum permittivity [23]) is equal to the laser frequency, $\omega_L$. Solid density Al is not relativistically transparent at the highest laser intensities achievable at present, for laser wavelength ∼1 $\mu$m. This is because the magnitude of $\gamma_e$ excited by the laser light is not sufficient to reduce the plasma frequency such that $\omega_{pe} < \omega_L$. However, when ultrathin foils are irradiated at laser intensities above $\sim 10^{20}$ Wcm$^{-2}$ they can undergo relativistic self-induced transparency (RSIT) due to expansion of the heated plasma electron population, reducing $n_e$ and thus $\omega_{pe}$ to below the threshold condition [24, 25]. When this occurs, the remainder of the laser pulse propagates through the expanding plasma, coupling energy to electrons across the interaction volume. This effectively changes the interaction physics from a critical density surface-dominated regime to a volumetric-coupling regime.

In this article, we report the first measurements of energy absorption for intense laser–foil interactions in the transition from a surface-dominated to a volumetric-dominated regime, by varying the target thickness from tens-of-microns to tens-of-nanometres. We find an optimum thickness for total energy absorption, but also measure the highest energy coupling to fast electrons for the thinnest targets investigated. Particle-in-cell (PIC) simulations indicate that there is significant direct laser acceleration of electrons occurring in the volumetric-dominated interaction regime.

## 2. Methodology

### 2.1. Experiment

The experiment was performed using the PHELIX laser [26] at the GSI laboratory, near Darmstadt in Germany. Linearly polarised pulses, of $\lambda_L = 1.053$ $\mu$m light, of pulse length $\tau_L = (0.7 \pm 0.1)$ ps (full width at half maximum, FWHM) and energy $E_L = (80 \pm 5)$ J were incident along the target normal axis onto Al foil targets with thickness, $l$, varied in the range 40 nm to 20 $\mu$m. Each target was mounted across a 400 $\mu$m circular aperture at the centre of a 3 × 3 mm copper frame. The laser temporal-intensity contrast was measured to be $10^{-12}$ at 1 ns and $10^{-4}$ at 10 ps, prior to the peak of the pulse [27]. Utilising a $f/1.5$ off-axis focussing parabola to direct a 15 cm diameter beam onto the target, a focal spot size, $\phi_L = (5 \pm 1)$ $\mu$m was achieved, resulting in an intensity $I_L = (9 \pm 3) \times 10^{19}$ W cm$^{-2}$. Figure 1(a) shows a schematic of the experiment arrangement.

To quantify the light absorbed during the interaction, the total energy reflected from, and transmitted through, the target was measured. A custom-made integrating sphere was used to capture the light over most of the solid angle and the uniform light field produced via multiple internal reflections was sampled using two fully-calibrated optical spectrometers [28]. Example spectral measurements of laser light diffusely scattered by the target or transmitted through it and collected by the integrating sphere are shown in figure 1(b), for two example target thicknesses, $\ell = 76$ nm and $\ell = 1$ $\mu$m. Light reflected back through the aperture for the incoming focussing laser beam was collected and imaged on a diffuse scatter screen placed behind the final turning mirror. Figure 1(c) shows a plot of the ratio of the diffusely scattered or transmitted energy to the energy of the laser light reflected back through the aperture, as a function of target thickness. In all cases, the measurements are an integration over $\pm$50 nm with respect the central wavelength of the fundamental. Higher harmonics are not included. Consistent with the definition used in Ping *et al* [19], we define the laser absorption as $E_{\mathrm{Abs}} = E_{\mathrm{L}} - E_{\mathrm{S}} - E_{\mathrm{BR}}$, where $E_{\mathrm{L}}$, $E_{\mathrm{S}}$ and $E_{\mathrm{BR}}$ are the energies of the incident laser pulse, the total light measured in the sphere (scattered from the target and transmitted through the target) and laser light back-reflected through the aperture, respectively. A 'wrap-around' stack of Fujifilm Image Plates was used to characterise the angular and energy distributions of the fast electrons that escape the plasma [29, 30]. The angular range of the detector was set by the experimental configuration to be $-90°$ to $+50°$, where $0°$ represents the laser axis. We utilise four layers of Image Plates, filtered with iron foils such that the minimum electron energy detected on respective layers was 4.5, 8.0 and 12.5 MeV. The measured photostimulated luminescence (PSL) values of the energy stored in the Image Plates is linearly correlated to the number of electrons depositing energy at each of these threshold values [31]. Further details of the experiment, including the calibration of the energy response of the diagnostics, is provided in reference [20].

### 2.2. Simulations

A programme of 2D PIC simulations was performed using the fully relativistic EPOCH code [32]. Linearly polarised (in the transverse spatial simulation plane) laser pulses with a Gaussian temporal and spatial profile of $\tau_{\mathrm{L}} = 0.55$ ps (FWHM) and $\phi_{\mathrm{L}} = 5$ $\mu$m (FWHM), respectively, were incident onto the target surface along the target normal axis, to produce a peak intensity equal to $6 \times 10^{19}$ W cm$^{-2}$. The plasma was initialised as a slab of solid-density $Al^{11+}$ ions ($60n_{\mathrm{c}}$, where $n_{\mathrm{c}}$ is defined as the non-relativistic critical electron density where $\omega_{\mathrm{pe}} = \omega_{\mathrm{L}}$) with thickness, $l$, varied in the range 20 nm to 6 $\mu$m and with a fixed 10 nm-thick layer of contaminant protons ($60n_{\mathrm{c}}$) on the front and rear sides. A corresponding electron population with a peak density of $660n_{\mathrm{c}}$ was initialised to neutralise the ions. The electrons have an initial temperature equal to 10 keV, while both ion species are set to 10 eV. The simulation box was 130 $\mu$m $\times$ 72 $\mu$m, using 26 000 $\times$ 6864 mesh cells, respectively, and the boundaries were all defined as free space.

To quantify the absorption, the unabsorbed laser field was determined throughout the simulated interaction. To this end, a spatial Fourier transform was applied to the electric fields (both the $X$ and $Y$ components). A bandpass filter was then applied to the resultant frequency spectrum around the laser frequency to remove the influence of both the slowly varying fields that grow within the target and extend into the surrounding vacuum and the highly localised fields associated with accelerated particles. An inverse Fourier transform was then performed on the resulting spectra to give a spatial grid of all electric field oscillations on the order of the laser frequency. The incoming laser field itself, as determined from a simulation without a target/plasma, was then subtracted. The resulting electric field values were spatially sampled in an annulus with inner and outer radius equal to 20 $\mu$m and 23 $\mu$m, respectively, centred on the focal spot region. The difference in radii is chosen to be the distance light will travel in between two simulation outputs to avoid oversampling. This was done to ensure the full focussing beam is captured as it travels towards the target, along with the portion that was either reflected or transmitted. A ratio of the magnitude of these field components to the incoming laser field then represents the absorption value. This provides a comparable measure to that obtained experimentally using the integrating sphere. We also tested an alternative approach in which the final energies of all particles and fields in the simulation were directly extracted. However, this does not provide an accurate absorption value due to particle loss from the simulation boundaries. For completeness, the results of this exercise, which provide an indication of energy partition, are available as supplementary material (stacks.iop.org/NJP/22/053044/mmedia).

## 3. Absorption and fast electron generation

Figure 2(a) shows the measured absorption as a function of $l$ in the range 77 nm to 20 $\mu$m. It is observed to vary from $\sim$65% to a peak of $\sim$80% at $l \sim 380$ nm (the foil thickness was 376 $\pm$5 nm). The simulation results are in good overall agreement, both in terms of the degree of absorption and the variation with target thickness. The simulations reveal that the optimum thickness ($l \sim 380$ nm) corresponds to the

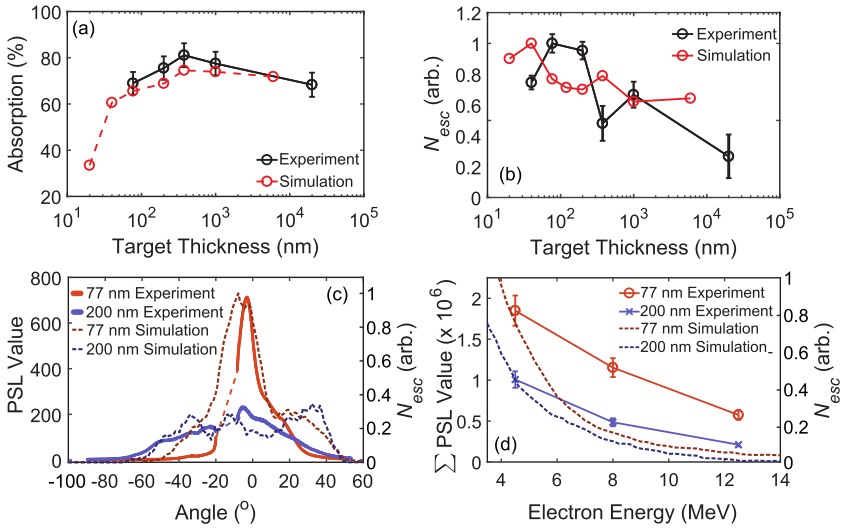


**Figure 2.** (a) Percentage laser energy absorption as a function of target thickness in the experiment (black) and PIC simulations (red). (b) Number of fast electrons escaping the plasma as a function of target thickness in the experiment (black) and PIC simulations (red). (c) Measured angular distribution of the total energy (PSL signal detected) of the escaping electrons on the final Image Plate layer (solid line) for two example target thicknesses, plotted alongside corresponding escaping electron angular distributions from the PIC simulations (dashed lines). (d) Total energy (PSL value) as a function of minimum electron energy for each layer of Image Plate in the stack, sampled in a circle with angular radius of 2.5°, for the same two example target thicknesses. Corresponding escaping electron spectra from the PIC simulations are included.

thinnest target that does not become relativistically transparent during the interaction, i.e. the target expands during the interaction such that the peak density is near (but remains higher than) the relativistically corrected critical density. The range of $l$ explored in the simulations was extended down to 20 nm, and it is found that at this value there is a sharp decrease in absorption, resulting from RSIT occuring very early in the interaction, and thus a large degree of laser transmission [13].

In figure 2(b), the total number of electrons measured by summing over a fixed area (spanning the full angular range of the Image Plate in the plane of the interaction and $\pm 2.5^\circ$ in the orthogonal plane) of the last three layers of Image Plate is plotted as a function of target thickness. Overall, the electron number increases with decreasing target thickness and corresponding results from the PIC simulations show a similar trend. There is a turning point at which the escaping electron numbers decrease at the thinnest targets explored experimentally and numerically. This arises due to the target undergoing RSIT early in the interaction, as well as a reduction in the overall available number of electrons in the interaction region. This is discussed further in later sections. There is also a measured decrease in the escaping electron signal in the thickness region just higher than the threshold for RSIT to occur ($l \sim 380$ nm). This is likely to arise because surface absorption mechanisms are less efficient at coupling energy to fast electrons due to plasma expansion, but volumetric energy coupling to electrons is not yet efficient as the laser pulse is not transmitted through the target.

Figure 2(c) shows the signal from the last Image Plate layer (corresponding to electrons with energy $>$ 12.5 MeV) plotted as a function of emission angle, for two example (stated) target thicknesses. The break in the measurement between $-10^\circ$ and $-20^\circ$ results from a gap in the Image Plate stack (to facilitate target alignment). The angular distribution of the electron beam is generally broad, but becomes narrow and more peaked for the thinnest targets (e.g. $l = 77$ nm). This is indicative of the electron distribution becoming more beamed, i.e. emitted over a narrow angular range, when RSIT occurs early in the interaction. The same effect is observed in the escaping electron population in the PIC simulations, as also shown in figure 2(c). It is consistent with previous work suggesting the formation of a narrow relativistic jet (or filament) of fast electrons in ultrathin foil targets undergoing RSIT [16–18].

The effective electron beam temperature can be obtained by measuring the change in the total energy deposited in a fixed region of Image Plate across each of the layers, as detailed in references [29, 30]. The total signal measured in a circle with angular radius of 2.5° around the laser axis for each of the final three layers is shown in figure 2(d) for the same two example thicknesses. There is little change in the beam temperature, but there is a clear increase in the number of electrons accelerated from the thinnest foils. The corresponding spectra from the PIC simulation results exhibit similar trends. We note that a direct comparison between the electron spectra from the simulation results and the measured electron signal in the three layers of Image Plate is not appropriate because the latter is not a deconvolved spectrum. However,

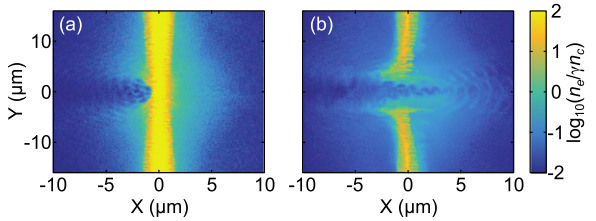


**Figure 3.** PIC simulation results showing the spatial distribution of the electron density as a ratio of the relativistically corrected critical density, 0.1 ps after the arrival of the peak of the laser pulse, for (a) $l = 376$ nm and (b) $l = 40$ nm Al. The laser enters from the left-hand boundary along the $Y = 0$ axis and is observed to interact with the critical density surface at the front side of the target, corresponding to a surface-dominated interaction in (a), and to propagate through the target, corresponding to volumetric interaction, in (b).

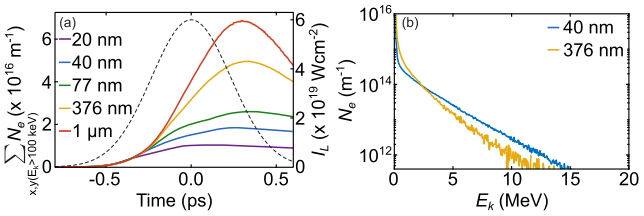


**Figure 4.** PIC simulation results showing (a) the number of electrons with energy greater than 100 keV as a function of time for given target thicknesses, and (b) the electron energy spectrum for the full electron population for two target thicknesses at time $t = 0$ ps (i.e. when the peak of the laser pulse interacts with the centre of the target). The laser temporal intensity profile at the target front surface is plotted in (a) for reference.

both show that more electrons are produced at high energies. Measured electron angular and energy distributions for additional target thicknesses are provided as supplementary material.

## 4. Effects of RSIT on electron acceleration

To investigate the effects of RSIT on electron acceleration, we examine the simulation results for two cases, $l = 376$ nm, which remains opaque (above the thickness threshold for RSIT to occur), and $l = 40$ nm, for which RSIT occurs near the peak of the laser pulse interaction. The spatial distribution of the fast electron density is plotted (normalised to the relativistically corrected critical density), at 0.1 ps after the peak of the laser pulse, in figure 3(a) and (b). It is clear that for the $l = 40$ nm case, along the laser axis the relativistically corrected electron density drops below the threshold for transparency ($n_e/\gamma_e < n_c$), enabling the remainder of the laser pulse to propagate and interact directly with electrons over the full thickness of the expanding plasma. The $l = 376$ nm target remains opaque to the laser light throughout the interaction and so the laser pulse predominantly interacts with the critical density surface at the front side of the plasma.

Although the change in total absorption varies relatively weakly with target thickness, the dynamics of the electrons accelerated by the laser are found to vary strongly. Figure 4(a) shows the number of electrons with energy >100 keV (i.e. significantly accelerated above their initial starting temperature of 10 keV) for given target thicknesses as a function of time, where time $t = 0$ denotes the arrival of the peak of the laser pulse at $X = 0$ (i.e. the centre of the target). An outline of the pulse profile is included to indicate the variation with time of the input laser intensity at the target. After an initial increase, the thinnest targets exhibit an effective saturation in the number of electrons with energy above the initial thermal distribution. This indicates that the electron population is quickly heated by the laser and further energy coupling is limited by the numbers of electrons available. By contrast, the numbers of electrons accelerated for the two thickest target cases ($l = 376$ nm and $l = 1$ $\mu$m) follows a trend similar to the intensity of the laser pulse profile, albeit delayed by ~300 fs. The highest gradient of increase in the number of high energy electrons is achieved at the peak of the pulse interaction. For the case of the thinnest target, $l = 20$ nm, 44% of the total electron population in the simulation is accelerated, whilst the corresponding fraction is only 5% for the $l = 1$ $\mu$m case. The significantly larger number of electrons available for the thicker target enables higher overall energy coupling to electrons.

Figure 4(b) compares the energy spectrum of the full electron population as the peak of the pulse interacts with the target for $l = 40$ nm and $l = 376$ nm. The $l = 40$ nm target has undergone RSIT at this point in time. The numbers of sub-MeV electrons are higher for the opaque $l = 376$ nm target due to the

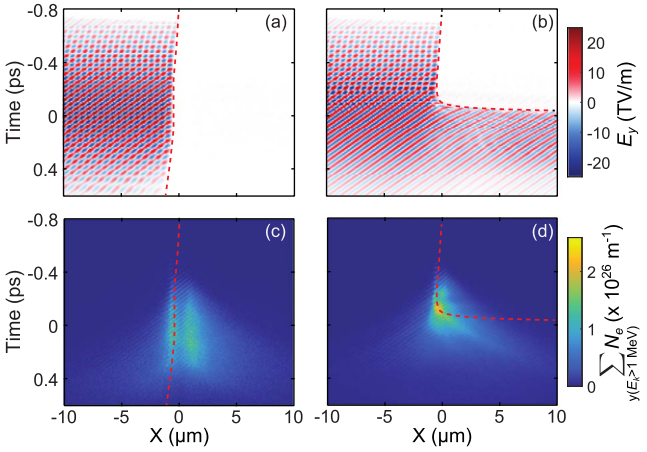


**Figure 5.** PIC simulation results showing the transverse electric field strength along the laser propagation axis as a function of time, for (a) $l = 376$ nm and (b) $l = 40$ nm Al targets. Corresponding plots for the number of electrons with kinetic energy greater than 1 MeV for (c) $l = 376$ nm and (d) $l = 40$ nm. $t = 0$ ps corresponds to the arrival of the peak of the laser pulse at $X = 0$ in the absence of plasma. The red dash marks the extent of the laser light propagation in $X$.

higher number of electrons available for acceleration. By contrast, the numbers of electrons with energy >2 MeV are higher for the $l = 40$ nm target (consistent with the results in figure 2(d)).

The transverse electric field (dominated by the laser itself) along the longitudinal axis of the simulation box, i.e. the laser propagation axis, is shown in figure 5(a) and (b) for $l = 376$ nm and $l = 40$ nm, respectively. The dashed red line denotes the extent of the laser light propagation in $X$. The $l = 376$ nm target is observed to remain opaque throughout the interaction, with the laser light reflecting from the critical density surface. By contrast, as the laser intensity ramps up, the laser light is observed to propagate through the expanding $l = 40$ nm target just before the peak of the interaction ($t = 0$). It should be noted that due to the temporal output rate of the simulation, the laser fields shown are under-sampled and suffer from aliasing. Nonetheless, this still provides an adequate guide for the laser propagation and highlights the clear difference in laser propagation in the case of these two targets.

It can also be seen, for both targets, that early in the interaction there is a standing wave-like field formed due to the reflection of the laser pulse from the critical density surface. As the laser intensity increases, changes in the field distribution are observed for both targets. The standing wave disappears for the case of the $l = 40$ nm target when it becomes relativistically underdense and the laser propagates through. However, for both targets the standing wave pattern starts to change from $t = -0.4$ ps, which indicates a reduction in reflected energy due to increasing absorption. For the $l = 376$ nm case, because RSIT does not occur, the absorption is strong over the remainder of the pulse, including the high intensity temporal portion of the pulse. Figures 5(c) and (d) show the corresponding numbers of electrons with energy >1 MeV (integrated in the $Y$ dimension from $-2.5$ $\mu$m to 2.5 $\mu$m) for the $l = 376$ nm and $l = 40$ nm cases, respectively. For $l = 376$ nm, these high energy electrons are generally trapped within the target, refluxing or recirculating between the electrostatic fields that build up on the surfaces [20, 21, 33]. For the $l = 40$ nm target, shortly before the arrival of the peak of the laser pulse a population of relativistic electrons are accelerated and propagate forward with the laser light (this corresponds to the time at which the target becomes relativistically transparent). Both the maximum energy and number of high energy electrons escaping the target are higher for the thinner target case.

The $l = 40$ nm foil expands during the early part of the laser pulse interaction, to produce a near critical density plasma (with density gradients) extending over microns. These conditions result in direct laser acceleration (DLA) of electrons as the remainder of the laser pulse propagates through the plasma. DLA has been investigated previously in the case of uniform near critical density plasma [34, 35]. The main driver for DLA is the formation of strong longitudinal electric field structures due to self-focusing of the laser pulse and reflection from the overdense regions of the plasma [36]. To demonstrate this effect, the longitudinal electric fields are plotted in figures 6(a) and (b) for $l = 376$ nm and $l = 40$ nm, respectively, sampled at $t = 0.2$ ps. For $l = 376$ nm, longitudinal field structures are limited to a region at the front of the target, but form throughout the laser propagation axis for the $l = 40$ nm case. This results in a boost in the average electron energies for the case of the thinner target, as demonstrated in figures 6(c) and (d). For the $l = 376$ nm case, electrons are accelerated at the target front surface and injected into the overdense plasma bulk where the laser field does not extend. For the thinner target case, fast electron bunches are observed across the laser propagation axis, leading to higher average energy electrons being ejected from the target.

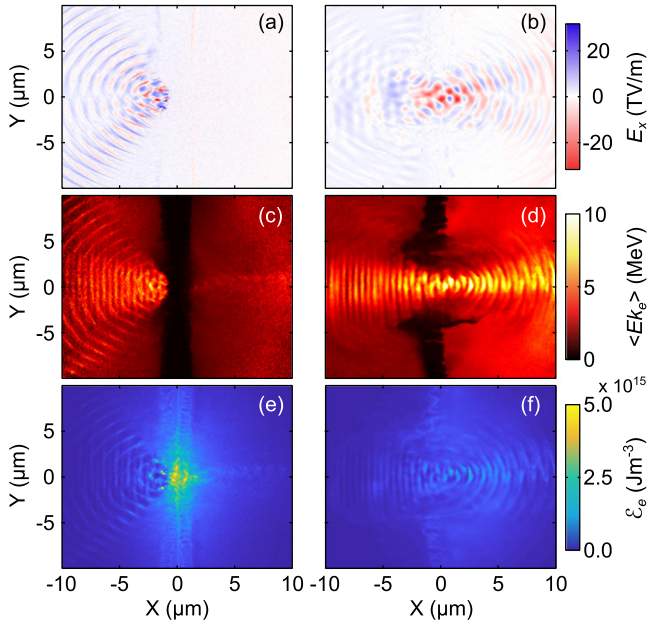


**Figure 6.** PIC simulation results showing the longitudinal $E_X$ field for (a) $l = 376$ nm and (b) $l = 40$ nm, the average electron energy for (c) $l = 376$ nm and (d) $l = 40$ nm, and the total electron energy density $\mathcal{E}_e$ for (e) $l = 376$ nm and (f) $l = 40$ nm. All plots are sampled at $t = 0.2$ ps.

The total electron energy density at the same point in time is shown in figures 6(e) and (f) for $l = 376$ nm and $l = 40$ nm, respectively. In the case of the thicker target, the fast electrons become trapped and recirculate within the target between the longitudinal sheath fields formed on both surfaces, leading to the majority of the electron energy being contained within the overdense plasma bulk. For $l = 40$ nm, the majority of the energy is contained in the directly accelerated electron bunches, but with reduced total energy due to the limited number of electrons available.

## 5. Influence of target pre-expansion driven by the laser intensity contrast

The measurements and simulation results discussed thus far involve fixed laser pulse temporal-intensity contrast. The precise target thickness at which the changeover from surface- to volume-dominated absorption processes occurs will depend on the degree of target expansion (from initial solid density) prior to the arrival of the main laser pulse. Such preformed plasma is induced at the point in the time at which the laser amplified spontaneous emission (ASE) pedestal or any prepulses present exceed the threshold for ionisation. To explore the influence of this effect for the parameters of the main laser pulse in this study, additional PIC simulations were performed in which the initial target foil was pre-expanded. This was achieved by defining each target as a 1D Gaussian density profile in the laser propagation direction (i.e. along the $X$-axis of the simulation) for two example cases with the Gaussian FWHM defined as $d_{\mathrm{exp}} = 400$ nm and $d_{\mathrm{exp}} = 800$ nm, and for $l$ in the range 20 nm to 1 $\mu$m. $d_{\mathrm{exp}} = 0$ nm is defined as the initially unexpanded case used in all of the results above and the upper limit of $d_{\mathrm{exp}} = 800$ nm was chosen such that the $l = 20$ nm target equivalent would still be overdense when the main pulse arrived. The areal density of the electrons and ions was conserved for solid density targets in the range 20 nm to 1 $\mu$m, which results in a decrease of the peak electron density for targets for which $l < 200$ nm. For $l > 200$ nm, the density was capped at solid density ($\sim 630\, n_c$) and the target extended at this density such that the areal density is conserved.

Figure 7 shows the results, demonstrating the effect of pre-expansion on laser energy absorption and coupling to fast electrons that escape the plasma. The overall trends do not change and in particular the absorption decreases by less than 5%. The escaping electron numbers vary significantly only at areal density $\sim 2 \times 10^3 \mu\mathrm{gcm}^{-2}$, corresponding to $l = 376$ nm, which is the target thickness near the threshold for the onset of RSIT. Thus, the degree of pre-expansion of the target changes the precise initial target thickness at which volumetric coupling of laser energy to electrons occurs, but does not change the conclusions reached above.

The lack of appreciable difference in the absorption arises because early in the interaction with the main laser pulse (on the rising edge) the target that starts with no prior expansion quickly expands to a level

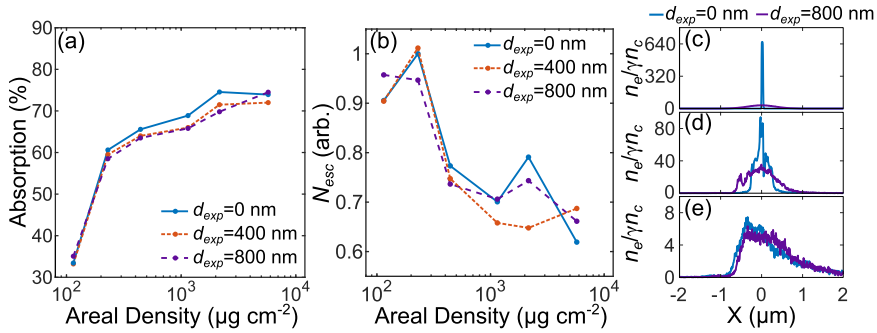


**Figure 7.** PIC simulation results. (a) Laser energy absorption as a function of target areal density for three cases of initial target expansion: $d_{\rm exp} = 0$ nm, $d_{\rm exp} = 400$ nm and $d_{\rm exp} = 800$ nm. (b) Escaping electron number as a function of target areal density for the same three initial expansion cases. (c)–(e) Electron density profile for initial expansion $d_{\rm exp} = 0$ nm and $d_{\rm exp} = 800$ nm ($l = 40$nm) cases, along the laser propagation axis ($Y = 0$ $\mu$m), at interaction time: (c) $t = -0.7$ ps (starting condition); (d) $t = -0.4$ ps; and (e) $t = -0.1$ ps.

similar to that of the pre-expanded cases. This can be seen in the comparison of the evolution of the electron density profiles for the $d_{\rm exp} = 0$ nm and $d_{\rm exp} = 800$ nm ($l = 40$ nm) cases shown in figures 7(c)–(e). Before the peak of the laser pulse arrives ($t = 0$), the electron density profile for both cases are very similar, as observed in figure 7(e). We note that the overall scale length of the plasma is of the order of, or less than, the laser wavelength and thus propagation instabilities and related phenomena that can significantly change absorption do not occur.

## 6. Summary

In summary, we report the first measurements of total laser energy absorption as a function of target thickness in the transition from surface- to volume-dominated relativistic laser–foil interactions. Absorption is highest in targets with thickness just above the threshold for relativistic transparency to occur. Our simulations indicate an effective balance between the number of available electrons that the laser can accelerate, which is limited by the target thickness, and the maximum energy these electrons can reach. In the case of surface-dominated interactions, the overall laser energy absorption is high, but the majority of the electron energy is contained within the target due to reflection of electrons in the sheath electrostatic fields formed at the front and rear sides resulting in recirculation. For targets that become relativistically transparent relatively early in the interaction, giving rise to volumetric interactions as the remainder of the laser pulse propagates through the expanded near critical density plasma, direct acceleration of electrons occurs. The total energy coupling to electrons is lower than that of the targets which do not achieve RSIT, but a larger number of high energy electrons escape the target, and in a more directed beam.

These findings enhance our understanding of energy absorption and coupling to fast electrons in the relativistic self-induced transparency regime, and thus inform the development of hybrid schemes for ion acceleration [13] and the generation of high density directed beams of fast electrons, and by extension photons and neutrons [37].

## Acknowledgments

We acknowledge the expertise of the PHELIX laser staff at the GSI laboratory. This research is financially supported by EPSRC (grant numbers EP/R006202/1, EP/M018091/1 and EP/K022415/1) and used the ARCHER and ARCHIE-WeSt high performance computers, with access to the former provided via the Plasma Physics HEC Consortia (EP/R029148/1). EPOCH was developed under EPSRC grant EP/G054940/1. This project has received funding from the European Union's Horizon 2020 research and innovation program under grant agreement No 654148 Laserlab-Europe. Data associated with research published in this paper can be accessed at https://doi.org/10.15129/228600b8-f6f9-444f-8156-09188702d006.

## ORCID iDs

R J Gray https://orcid.org/0000-0003-0610-9595
M King https://orcid.org/0000-0003-3370-6141
R Wilson https://orcid.org/0000-0003-4835-3262
C Armstrong https://orcid.org/0000-0002-0157-3746
P McKenna https://orcid.org/0000-0001-8061-7091

## References

[1] Macchi A, Borghesi M and Passoni M 2013 *Rev. Mod. Phys.* **85** 751–93
[2] Daido H, Nishiuchi M and Pirozhkov A S 2012 *Rep. Prog. Phys.* **75** 056401
[3] Roth M *et al* 2013 *Phys. Rev. Lett.* **110** 044802
[4] Kar S *et al* 2016 *New J. Phys.* **18** 053002
[5] Chen H, Wilks S C, Bonlie J D, Liang E P, Myatt J, Price D F, Meyerhofer D D and Beiersdorfer P 2009 *Phys. Rev. Lett.* **102** 105001
[6] Sarri G *et al* 2015 *Nat. Commun.* **6** 6747
[7] Norreys P A *et al* 1999 *Phys. Plasmas* **6** 2150–6
[8] Tabak M, Hammer J, Glinsky M E, Kruer W L, Wilks S C, Woodworth J, Campbell E M and Perry M D 1994 *Phys. Plasmas* **1** 1626–34
[9] McKenna P *et al* 2011 *Phys. Rev. Lett.* **106** 185004
[10] MacLellan D A *et al* 2014 *Phys. Rev. Lett.* **113** 185001
[11] Yin L, Albright B J, Hegelich B M and Fernndez J C 2006 *Laser Part. Beams* **24** 291–8
[12] Hegelich B M *et al* 2013 *New J. Phys.* **15** 085015
[13] Higginson A *et al* 2018 *Nat. Commun.* **9** 724
[14] Gonzalez-Izquierdo B *et al* 2016 *Nat. Phys.* **12** 505–12
[15] Gonzalez-Izquierdo B *et al* 2016 *Nat. Commun.* **7** 12891
[16] Powell H W *et al* 2015 *New J. Phys.* **17** 103033
[17] Palaniyappan S, Huang C, Gautier D C, Hamilton C E, Santiago M A, Kreuzer C, Sefkow A B, Shah R C and Fernndez J C 2015 *Nat. Commun.* **6** 10170
[18] King M *et al* 2016 *Nucl. Instrum. Methods Phys. Res.* A **829** 163–6
[19] Ping Y *et al* 2008 *Phys. Rev. Lett.* **100** 085004
[20] Gray R J *et al* 2018 *New J. Phys.* **20** 033021
[21] Sentoku Y, Cowan T E, Kemp A and Ruhl H 2003 *Phys. Plasmas* **10** 2009–15
[22] Kruer W L and Estabrook K 1985 *Phys. Fluids* **28** 430–2
[23] Chen F 1984 *Introduction to Plasma Physics and Controlled Fusion* 2nd edn vol 1 (New York: Plenum)
[24] Vshivkov V A, Naumova N M, Pegoraro F and Bulanov S V 1998 *Phys. Plasmas* **5** 2727–41
[25] Eremin V I, Korzhimanov A V and Kim A V 2010 *Phys. Plasmas* **17** 043102
[26] Bagnoud V *et al* 2010 *Appl. Phys.* B **100** 137–50
[27] Bagnoud V and Wagner F 2016 *High Power Laser Sci. Eng.* **4** e39
[28] Buckley H 1921 *J. Inst. Electr. Eng.* **59** 143–52
[29] Gray R J *et al* 2011 *Appl. Phys. Lett.* **99** 171502
[30] Rusby D R *et al* 2015 *J. Plasma Phys.* **81** 475810505
[31] Chen H *et al* 2008 *Rev. Sci. Instrum.* **79** 033301
[32] Arber T D *et al* 2015 *Plasma Phys. Control. Fusion* **57** 113001
[33] Link A, Freeman R R, Schumacher D W and Van Woerkom L D 2011 *Phys. Plasmas* **18** 053107
[34] Arefiev A V, Khudik V N, Robinson A P L, Shvets G, Willingale L and Schollmeier M 2016 *Phys. Plasmas* **23** 056704
[35] Sorokovikova A, Arefiev A V, McGuffey C, Qiao B, Robinson A P L, Wei M S, McLean H S and Beg F N 2016 *Phys. Rev. Lett.* **116** 155001
[36] Willingale L *et al* 2018 *New J. Phys.* **20** 093024
[37] Pomerantz I *et al* 2014 *Phys. Rev. Lett.* **113** 184801